Chirality effects on channel modeling for THz-band wireless communications in LoS/NLoS propagation

Anna Maria Vegni, Valeria Loscrì

Chirality effects on channel modeling for THz-band wireless communications in LoS/NLoS propagation

Anna Maria Vegni[a,*], Valeria Loscrí[b]

[a]*Department of Engineering, Roma Tre University, Rome, Italy*
[b]*INRIA Lille-Nord Europe, FUN Research Lab, Lille Nord-Europe, France.*

Abstract

Channel modeling in the Terahertz frequency band has become a very hot research field, above all in the context of nano-Internet of Things. Thanks to the exploitation of frequencies in the interval ranging from 0.06 to 10 THz, it is envisioned the possibility to overcome the issues related to the spectrum scarcity and capacity limitation. On the other hand, the design of new channel models, able to capture the inherent features of the phenomenons related with this specific field is of paramount importance. Very high molecular absorption, and very high reflection loss are peculiarities phenomenons that need to be included in these models. In this paper, we present a *full-wave* propagation model of the electromagnetic field that propagates in the THz band both for Line-of-Sight and Non-Line-of-Sight propagation models. In the full-wave model, we also introduce the chirality effects occurring in the propagation medium, *i.e.*, a chiral metamaterial. Finally, the analysis of path loss in Line-of-Sight and Non-Line-of-Sight propagation models, and for biological and indoor application scenarios, has been carried

*Corresponding author
Email addresses: annamaria.vegni@uniroma3.it (Anna Maria Vegni), valeria.loscri@inria.fr (Valeria Loscrí)

out through simulation results.

Keywords: Chirality effects, full-wave model, THz channel modeling, nanoscale communications

1. Introduction

The increasing demand of wireless communication systems based on large-scale use of nanodevices according to the Internet of Things idea has enhanced the attention on accurate and more precise channel models working in the Terahertz frequency band. This was a consequence of new sensing components to be used in a large variety of applications, including *e.g.* health and life sciences.

Nowadays, the Terahertz band [1] has been identified in the range $[0.06, 10]$ THz, and represents one of the most promising spectrum bands to enable ultra-high-speed communications. The use of this frequency band is envisioned to address the spectrum scarcity and capacity limitations of current wireless systems, thus providing a plethora of applications, like ultra-high-speed wireless communications.

In order to address these needs for an optimal wireless communication networks in the THz band, it is necessary to develop new channel models working in THz band, that include specific phenomenons that are more evident when working in optic and almost-optic frequencies [2]. Researchers are investigating specific Terahertz spectrum peculiarities, like the *very high molecular absorption loss* or the *very high reflection loss*. Indeed, differently from traditional lower frequency bands, where the propagation is mainly influenced by the spreading loss only, the physical mechanisms in a THz-band wireless transmission are a very high molecular absorption loss, and spreading loss. Also, the molecular absorption

attenuates the propagated signals in THz-band wireless communications. These phenomenons are specific for THz band and cause a very high and frequency-selective path loss for Line-of-Sight (LoS) links, while high reflections occur in Non-Line-of-Sight (NLoS) propagation due to the type of material and the roughness factor of reflecting surfaces [2, 3, 4].

From all these considerations, it follows that existing channel models used for lower frequency bands cannot be re-used for THz communications, and then the need to design novel channel models for THz band is a challenge. In this paper, we omit channel models for lower frequency (*i.e.*, ultra-wideband), but investigate recent works in channel modeling for THz band.

Many works have already investigated all these specific phenomenons occurring in the THz band, and consequently novel channel models for THz band have been presented so far. One of the main channel models for communications in THz band is that presented by Jornet and Akyildiz in [5], which includes both molecular absorption and free space loss. In [6], Llatser *et al.* investigate the influence of molecular absorption in a short-range THz communication model on both frequency and time domain. Piro *et al.* [7] address radio propagation models for nanoscale wireless communications in the field of nanomedicine. Finally, Boronin *et al.* [8] present a model for describing the phenomena of molecular noise occurring in THz band. This concept has been broadly surveyed in [9] by distinguishing from time and frequency dependence.

In [3] Moldovan *et al.* present a deterministic channel model working in THz band, both in case of LoS and NLoS propagation, and by assuming molecular absorption and spreading loss, together with a ray-tracing approach. In [4] Han *et al.* deal with a multi-ray channel model that considers not only LoS and NLoS

propagation effects, but also reflected, scattered and diffracted paths. This work represents an accurate channel model, where the use of ray tracing technique is exploited. Because of the very short wavelength in the THz band, THz waves propagate quasi-optically and can be modeled highly accurate with a ray optical approach. Ray tracing has already enabled good capabilities at low Terahertz frequency *i.e.*, at 0.3 THz.

In [10], Sheikh *et al.* use a ray-tracing model to simulate the multipath wave propagation in a realistic office environment, and include the frequency dependent atmospheric attenuation.

Another feature to be considered is the scattering effect. Piesiewicz *et al.* [11] study scattering properties of typical building materials, for channel modeling in THz band. The authors observed that in realistic environments, with rough surfaces, the modeling of the propagation effects should take into account the reduction of the reflected power in the specular direction due to diffuse scattering, even if not extremely large. Also, robust scattering models are needed and can be implemented in ray-tracing algorithms to enhance the propagation modeling. Finally, Kokkoniemi *et al.* [12] consider the scattering effect into the channel modeling in the THz band. They theoretically analyze multiple scattering effects, referring to a sequence of scattering events from small particles, such as aerosols. It is shown that the small particle scattering can result into significant additional loss that needs to be taken into account with the loss depending on the density and size distribution of the particles.

As can be noticed from previous works, the channel modeling in THz band is addressed through transfer functions that consider specific effects, like molecular absorption loss, spreading loss, reflected, diffracted, and scattered rays. However,

the *electromagnetic chirality effect* and the particular kind of the medium (also in terms of power excitation, with respect to the intensity of the electromagnetic field) are a few aspects that are often neglected in classical modeling of transmission channels. In fact, related works on channel modeling in the THz band consider the behavior of the channel by assuming molecular absorption loss function, the signal attenuation due to free space, and the particle scattering effect. All those aspects are assumed through appropriate functions (*e.g.* the Friis's function, the directivity of the transmitting antenna) added to the amplitude of the transmitted electromagnetic field. These features can be addressed in terms of constitutive relations of the electromagnetic medium, where the propagation of the electromagnetic signal occurs. On the other side, in this paper, we aim to consider a punctual setup of the issue, based on the determination of whole structure of the electromagnetic field that propagates in the channel, and then, a more appropriate definition of the constitutive relations of the medium should result important for this aim.

To summarize, the main goals addressed in this paper are (*i*) the full-wave propagation model in a non-conventional material (namely, a chiral metamaterial), and (*ii*) how the chirality effects affect the channel transfer functions on LoS and NLoS propagation. Chiral metamaterials, namely metamaterials that do not present any mirror symmetry plane, are materials where electric (magnetic) field generates also magnetic (electric) polarization [13]. They represent a very interesting category of metamaterials, since they offer great possibilities in the control of polarization such as optical activity. Specifically, they allow the polarization rotation of a linearly polarized wave.

As outlined in [14], another aspect really interesting of chiral metamaterials

is the exploitation of chirality property in order to reduce the attractive Casimir force, which is detrimental in micro- and nano-electromechanical systems. It has been discovered that chiral metamaterials are very good to realize the repulsive Casimir force, and this force is strictly dependent on the strength of the chirality. In particular, the repulsive force leads to nanolevitations and opens up many opportunities such as frictionless operation of nanomotors. Furthermore, chiral metamaterials can provide negative refractive index, and this type of materials has gained a lot of attention in the last few years, since they can be used in all the applications that require "perfect lenses", by overcoming diffraction limit.

This paper is organized as follows. In Section 2 we introduce a full-wave propagation model of the electromagnetic field that propagates in the THz band. Starting from the concept of electromagnetic chirality [15, 16, 17, 18], this approach considers the chiral effects following the change in the propagation velocity and in the refractive index, due to the chiral impurities inside the propagation medium. These effects are evaluated also in the case when the considered medium exhibits a Giant Optical Activity (GOA) [19, 20]. Section 3 describes the equivalent channel model by considering the chirality-affected channel transfer functions, both for LoS and NLoS propagation. In Section 4 the performances have been assessed in terms of path loss in cases of LoS and NLoS propagation mechanisms, for biological and indoor applications. Finally, conclusions are drawn at the end of the paper.

2. Full-Wave Propagation in THz Band

This section is devoted to the design of a full-wave propagation model for THz band. Starting from the classic harmonic macroscopic Maxwell's equations,

we consider the electromagnetic propagation inside a generic complex material, under the assumption that it is a linear and chiral medium.

Maxwell's equations represent the differential relations between the electric displacement $\mathbf{D}$ and the electric field $\mathbf{E}$, as well as the magnetic displacement $\mathbf{B}$ and the magnetic field $\mathbf{H}$, combined together with the constitutive relations characterizing the medium where the electromagnetic field exists according to assigned electric and magnetic sources.

For real-world materials, the constitutive relations are rarely simple, except approximately, and usually determined by experiment. For materials without polarisation and magnetisation effects (*i.e.*, vacuum), the constitutive relations are:

$$\mathbf{B} = \mu_0 \mathbf{H}, \quad \mathbf{D} = \varepsilon_0 \mathbf{E}, \tag{1}$$

where ε_0 is the electric permittivity, and μ_0 is the magnetic permeability.

For homogeneous materials, the electric permittivity is $\varepsilon = \varepsilon_0 \varepsilon_r$, where ε_r is the relative electric permittivity. Analogously, the magnetic permeability changes as $\mu = \mu_0 \mu_r$, where μ_r is the relative magnetic permeability. These quantities are constant throughout the material, while in inhomogeneous materials they depend on space location within the material. For isotropic materials, ε and μ are scalar quantities, while for anisotropic materials they are tensors *e.g.*, in crystal structures.

In this formulation unconventional materials (*i.e.* metamaterials) are also included, even if our considerations will be focused essentially on traditional dielectrics. Materials can be also generally dispersive, so that ε and μ depend on the frequency of any incident electro-magnetic (EM) waves. Even more generally, in the case of non-linear materials $\mathbf{B}$ and $\mathbf{D}$ are not necessarily proportional to $\mathbf{E}$,

and $\mathbf{H}$, respectively. In general, $\mathbf{D}$ and $\mathbf{B}$ depend on both $\mathbf{E}$ and $\mathbf{H}$, on location and time.

Now, let us consider a time-harmonic generic linear material, where chiral (magneto/electric-optical) effects are included in the following constitutive relations:

$$\begin{cases} \mathbf{B} = \underline{\xi} \bullet \mathbf{E} + \underline{\mu} \bullet \mathbf{H} \\ \mathbf{D} = \underline{\varepsilon} \bullet \mathbf{E} + \underline{\zeta} \bullet \mathbf{H} \end{cases} \tag{2}$$

where the symbol $\bullet$ represents the scalar product operator. In (2), $\underline{\xi}$, $\underline{\mu}$, $\underline{\varepsilon}$, and $\underline{\zeta}$ are specific tensor quantities of the material.

From (2) we observe the chirality property through the dependence of (*i*) $\mathbf{E}$ in $\mathbf{B}$, and (*ii*) $\mathbf{H}$ in $\mathbf{D}$. Furthermore, the displacement field existing inside the material is generated by an excitation expressed in terms of intensity of the incident electro-magnetic field. Therefore, the material under consideration is a linear chiral medium.

We remind that the chiral effects mean that:

- an electric field applied on the material provides not only an electric induction, but also a magnetic displacement,
- a magnetic field applied on the material provides not only a magnetic induction, but also an electric displacement,

unlike other non-chiral materials.

We assume this specific material with the aim of assessing the performance (*i.e.*, transmission of the electromagnetic power) of an optical channel. This performance is linked to the channel transfer function. Also, this formulation allows a more rigorous assessment of the channel properties, that is verified for all the frequency range (*i.e.*, from 0 to infinity).

For this aim, in our proposed approach we need to define the expressions of the EM field generated by a transmitter that is assumed as an impressed source distribution in a given volume V, characterized by assigned electric and magnetic vector functions $\mathbf{J}_{i,e}(\mathbf{r})$ and $\mathbf{M}_{i,m}(\mathbf{r})$ [1], respectively, where $\mathbf{r}$ is the observation vector. In the following, the spatial dependence $\mathbf{r}$ will be omitted.

The computation of the EM field in the channel is carried out through the solutions of linear differential equations, arising from the following Maxwell's equations:

$$\begin{cases} \nabla \times \mathbf{E} = -j\omega\mathbf{B} - \mathbf{M}_{i,m} \\ \nabla \times \mathbf{H} = j\omega\mathbf{D} + \mathbf{J}_{i,e} \end{cases} \tag{3}$$

where Kong's vector ∇ in Cartesian space has been used *i.e.*,

$$\nabla = \partial_x\hat{\mathbf{x}} + \partial_y\hat{\mathbf{y}} + \partial_z\hat{\mathbf{z}} = \frac{\partial}{\partial x}\hat{\mathbf{x}} + \frac{\partial}{\partial y}\hat{\mathbf{y}} + \frac{\partial}{\partial z}\hat{\mathbf{z}} \tag{4}$$

The system in (3) can be written as in the following form:

$$\begin{cases} \left(\underline{\nabla} + j\omega\underline{\xi}\right) \bullet \mathbf{E} = -j\omega\underline{\mu} \bullet \mathbf{H} - \mathbf{M}_{i,m} \\ \left(\underline{\nabla} - j\omega\underline{\zeta}\right) \bullet \mathbf{H} = j\omega\underline{\varepsilon} \bullet \mathbf{E} + \mathbf{J}_{i,e} \end{cases} \tag{5}$$

where Kong's operator $\underline{\nabla}$ is defined as a 3×3 matrix:

$$\underline{\nabla} = \begin{pmatrix} 0 & -\partial_z & \partial_y \\ \partial_z & 0 & -\partial_x \\ -\partial_y & \partial_x & 0 \end{pmatrix} \tag{6}$$

[1] The index i means impressed source distribution, e and m mean electric and magnetic, respectively.

and the solving differential equations for $\mathbf{E}$ and $\mathbf{H}$ are given, respectively:

$$\begin{cases} \left[\left(\underline{\nabla} - j\omega\underline{\zeta}\right) \bullet \underline{\mu}^{-1} \bullet \left(\underline{\nabla} + j\omega\underline{\xi}\right) - \omega^2\underline{\varepsilon}\right] \bullet \mathbf{E} = \mathbf{f}_e\left(\mathbf{J}_{i,e}, \mathbf{M}_{i,m}\right) \\ \left[\left(\underline{\nabla} + j\omega\underline{\xi}\right) \bullet \underline{\varepsilon}^{-1} \bullet \left(\underline{\nabla} - j\omega\underline{\zeta}\right) - \omega^2\underline{\mu}\right] \bullet \mathbf{H} = \mathbf{f}_m\left(\mathbf{J}_{i,e}, \mathbf{M}_{i,m}\right) \end{cases} \tag{7}$$

Equation (7) derives from well-known Maxwell's equations [21]. In this paper, we apply classical electromagnetic theory to the THz band, by assuming a signal generated by a linear polarized electric field propagating in a complex medium described by $\underline{\xi}$, $\underline{\mu}$, $\underline{\varepsilon}$, and $\underline{\zeta}$. Thus, from the authors' best knowledge, the following equations represent novel results, useful to derive the electromagnetic field in a complex medium. However, the proposed equations can be appropriately applied to both traditional and non-conventional (non-traditional) materials, under the assumption of specific material constitutive relations.

The solutions of the problem can be obtained via (7), together with the divergence equations. Following this approach, we obtain the expression of the total electromagnetic field, but in order to give a simplified formulation for every regular observation point P, that is $\forall \mathrm{P} \notin V$, we pose the condition of electric linear polarization (*e.g.*, $\hat{\mathbf{x}}$). Under this hypothesis, we get:

$$\begin{cases} \mathbf{E} = E_1\hat{\mathbf{x}} \\ \mathbf{H} = -\left(\rho_{R1} \bullet \xi_{R1}E_1\right)\hat{\mathbf{x}} + \left(j\frac{\rho_{23}}{\omega}\frac{\partial E_1}{\partial z} - \rho_{R2} \bullet \xi_{R1}E_1\right)\hat{\mathbf{y}} + \left(j\frac{\rho_{33}}{\omega}\frac{\partial E_1}{\partial y} + \rho_{R3} \bullet \xi_{R1}E_1\right)\hat{\mathbf{z}} \end{cases} \tag{8}$$

where ρ_{R1}, ρ_{R2}, and ρ_{R3} are the row vectors of $\underline{\rho} = \underline{\mu}^{-1}$ tensor, ξ_{R1} is the first row vector of $\underline{\xi}$ tensor, and ρ_{23}, ρ_{33} are elements of $\underline{\rho}$ tensor. Notice that $\mathbf{E}$ satisfies the

following partial differential equation:

$$f_1(\mathbf{r})\,E_1 + f_2(\mathbf{r})\,\frac{\partial E_1}{\partial x} + f_3(\mathbf{r})\,\frac{\partial E_1}{\partial y} + f_4(\mathbf{r})\,\frac{\partial E_1}{\partial z} + f_5(\mathbf{r})\,\frac{\partial^2 E_1}{\partial y^2} + f_6(\mathbf{r})\,\frac{\partial^2 E_1}{\partial z^2} = 0, \tag{9}$$

where functions $f_i(\mathbf{r})$ with $i = \{1, 2, \ldots, 6\}$ depend on the elements of $\underline{\xi}$, $\underline{\mu}$, $\underline{\varepsilon}$, and $\underline{\zeta}$ tensors, and assume complicated expressions. As an instance, we present the $f_1(\mathbf{r})$ term under the condition of spatial homogeneity of $\underline{\xi}$, $\underline{\mu}$, $\underline{\varepsilon}$, and $\underline{\zeta}$ tensors:

$$f_1(\mathbf{r}) = (\rho_{23} + \rho_{32}) \det \underline{\mathbf{\Omega}}_{1,1} + \omega^2 \left(\mathbf{v}_1 \bullet \underline{\xi}_{C1} - \varepsilon_{11}\right) \det \underline{\mathbf{\Omega}}_{1,2}, \tag{10}$$

with

$$\underline{\mathbf{\Omega}}_{1,1} = \begin{bmatrix} -\rho_{32} & \rho_{33} & \omega^2 \left(\underline{\zeta}_{R2} \bullet \underline{\rho}_{C1}\xi_{11} + \underline{\zeta}_{R2} \bullet \underline{\rho}_{C2}\xi_{21} + \underline{\zeta}_{R2} \bullet \underline{\rho}_{C3}\xi_{31} - \varepsilon_{21}\right) \\ \rho_{22} & -\rho_{23} & \omega^2 \left(\underline{\zeta}_{R3} \bullet \underline{\rho}_{C1}\xi_{11} + \underline{\zeta}_{R3} \bullet \underline{\rho}_{C2}\xi_{21} + \underline{\zeta}_{R3} \bullet \underline{\rho}_{C3}\xi_{31} - \varepsilon_{31}\right) \\ \left(\underline{\zeta}_{R1} \bullet \underline{\rho}_{C2}\right) & \left(-\underline{\zeta}_{R1} \bullet \underline{\rho}_{C3}\right) & 0 \end{bmatrix}, \tag{11}$$

$$\underline{\mathbf{\Omega}}_{1,2} = \begin{bmatrix} \rho_{13} & \rho_{32} & -\rho_{33} \\ -\rho_{12} & \rho_{22} & -\rho_{23} \\ \left(\underline{\zeta}_{R2} \bullet \underline{\rho}_{C2} - \underline{\zeta}_{R3} \bullet \underline{\rho}_{C3}\right) & \left(\underline{\zeta}_{R1} \bullet \underline{\rho}_{C2}\right) & \left(-\underline{\zeta}_{R1} \bullet \underline{\rho}_{C3}\right) \end{bmatrix}, \tag{12}$$

$$\mathbf{v}_1 = \underline{\zeta}_{R1} \bullet \underline{\rho}_{C1}\hat{\mathbf{x}} + \underline{\zeta}_{R1} \bullet \underline{\rho}_{C2}\hat{\mathbf{y}} + \underline{\zeta}_{R1} \bullet \underline{\rho}_{C3}\hat{\mathbf{z}}, \tag{13}$$

where the indexes $C1$, $C2$, and $C3$ represent the column vectors.

According to this approach, the Poynting's vector defined as:

$$\mathbf{P} = \frac{\mathbf{E} \times \mathbf{H}^*}{2}, \tag{14}$$

can be split into two components *i.e.*, $\mathbf{P} = P_y\hat{\mathbf{y}} + P_z\hat{\mathbf{z}}$, whose expressions are

$$\begin{cases} P_y = -\frac{E_1}{2}\left(j\frac{\rho_{33}}{\omega}\frac{\partial E_1}{\partial y} + \rho_{R3} \bullet \xi_{R1}E_1\right)^* \\ P_z = \frac{E_1}{2}\left(j\frac{\rho_{23}}{\omega}\frac{\partial E_1}{\partial z} - \rho_{R2} \bullet \xi_{R1}E_1\right)^* \end{cases} \tag{15}$$

From (15), we can easily distinguish that Poynting's vector is formed by two components that are orthogonal to each other (*i.e.*, P_y and P_z), and to the electric polarization axis (*i.e.*, $\hat{\mathbf{x}}$). Therefore, if we refer this solution to the case of a transmission channel, where a giant optical activity could be activated, we can deduce that one of these terms is responsible of LoS power (W^{LoS}), that is the power at the receiver traveling along the direct (LoS) path, and the other one contributes to the NLoS power (W^{NLoS}), that is the power at the receiver traveling along the indirect (NLoS) path, according to the receiver location. Obviously, similar considerations hold for a $\hat{\mathbf{y}}$/$\hat{\mathbf{z}}$-axis electric polarization.

In the following, we attribute the presence of the indirect path as due at reflection/scattering/diffraction centers located at $z = h$. Therefore, the reflection/scattering/diffraction characteristics of the transmissive channel can be evaluated through the specific knowledge of the local planar geometry associated to these centers. In this paper, we consider the effects of the reflection generated by these centers allocated in the generic S points, while diffraction coefficient requires the knowledge of the canonical geometry of the diffraction points. This consideration limits the cases of real geometry that can be examined, and imposes a statistical approach to the problem more than a deterministic one we are dealing with. Finally, scattering effects can be inserted either at the level of constitutive relations or added in dB as a global term to the power flow evaluation.

By assuming Figure 1, where the transmitter and the receiver are aligned along

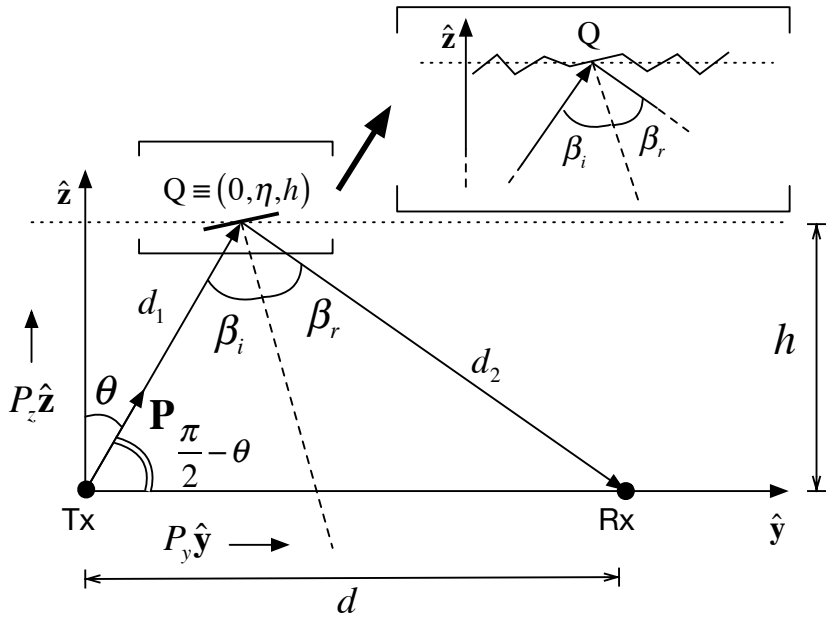

Figure 1: Schematic of the reference geometry, where the transmitter (Tx) and the receiver (Rx) lay along the $\hat{\mathbf{y}}$-axis with the generic reflecting point Q belonging to $\{x = 0, z = h\}$.

the $\hat{\mathbf{y}}$-axis, we can derive that the LoS power (*i.e.*, W^{LoS}) is determined by P_y, while the NLoS power (*i.e.*, W^{NLoS}) is contributed both by P_y, and P_z.

So, at the receiver the W^{LoS} can be written as

$$\begin{aligned} W^{\mathrm{LoS}} &= \int_{S_R} \hat{\mathbf{n}} \bullet P_y \hat{\mathbf{y}} dS = \\ &= \tfrac{1}{2} \int_{S_R} \left[j \tfrac{\rho^*_{33}}{\omega} E_1 \tfrac{\partial E^*_1}{\partial y} - \rho^*_{R3} \bullet \xi^*_{R1} E_1 E^*_1 \right] \Big| dS, \end{aligned} \tag{16}$$

being $\hat{\mathbf{n}}$ the normal vector to the S_R receiving surface *i.e.*, $\hat{\mathbf{n}} = -\hat{\mathbf{y}}$.

We observe that (16) is a general formula that can be applied in the case of conventional and/or unconventional materials. In this way it can be applied either to biological propagation media, as well as indoor wireless communications. Moreover, (16) is expressed in terms of the electric field and depends on the ele-

ments of the constitutive tensors. The explicit representation of the electric field can be obtained after integration of (9), as it will be indicated below.

On the other side, in order to obtain the W^{NLoS}, we need to evaluate the indirect path followed by the Poynting's vector through the generic reflection/ scattering/ diffraction point S laying in the $z = h$ plane, to reach the receiving point.

We distinguish these points S into two classes *i.e.*, (*i*) Q points belonging to the straight line $(x = 0, z = h)$, and (*ii*) all the remaining R points in the $z = h$ plane. In this paper, we refer to the first class Q points, as shown in Figure 1.

Let us consider the effect of the local mirror reflection in points Q in $z = h$. In this generic reflection point, the dielectric discontinuities in the permittivity give a local specular reflection coefficient that acts on the two incident Poynting's vectors $\mathbf{P}^{(i)}$ components *i.e.*, $\mathbf{P}^{(i)} = {P_y}^{(i)}\hat{\mathbf{y}} + {P_z}^{(i)}\hat{\mathbf{z}}$, and is depending on the specific location of point Q and the reflecting local plane. This local specular reflection coefficient generates the reflected Poynting's vector $\mathbf{P}^{(r)} = {P_y}^{(r)}\hat{\mathbf{y}} + {P_z}^{(r)}\hat{\mathbf{z}} = {P_y}^{\mathrm{NLoS}}\hat{\mathbf{y}} + {P_z}^{\mathrm{NLoS}}\hat{\mathbf{z}}$, in the NLoS path, contributing to W^{NLoS}.

From Figure 1, it is easy to verify that for Q points belonging to the $z = h$-plane, the incident/reflected β angle, related to the incident Poynting's vector, is connected to the elevation angle θ by the following simple relation:

$$\frac{\cos\theta}{\cos(\theta - 2\beta)} = \frac{d_2}{d_1}, \tag{17}$$

where d_1 and d_2 are the distances of these points from the transmitter and the receiver, respectively. Notice that for R points, a similar formula for the NLoS $\hat{\mathbf{y}}$-axis Poynting's vector component can be established as well.

Let us now determine $\mathbf{P}^{(r)}$ in Q points. With reference to Figure 2 (*a*), we can

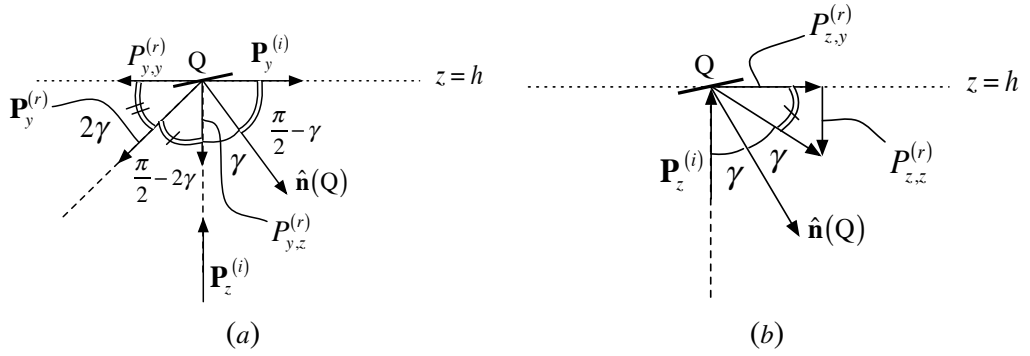

Figure 2: Schematic of the reference geometry for $\mathbf{P}^{(r)}$ evaluation, in the case of (*a*) $\mathbf{P}_y^{(i)}$, and (*b*) $\mathbf{P}_z^{(i)}$ components.

write:

$$\begin{aligned}
&\mathbf{P}^{(r)}\big|_{\mathrm{Q}} = P_y{}^{(r)}\Big|_{\mathrm{Q}}\hat{\mathbf{y}} + P_z{}^{(r)}\Big|_{\mathrm{Q}}\hat{\mathbf{z}} = \\
&= \left(-P_{y,y}{}^{(r)} + P_{z,y}{}^{(r)}\right)\Big|_{\mathrm{Q}}\hat{\mathbf{y}} - \left(P_{y,z}{}^{(r)} + P_{z,z}{}^{(r)}\right)\Big|_{\mathrm{Q}}\hat{\mathbf{z}} = \\
&= P_y{}^{\mathrm{NLoS}}\big|_{\mathrm{Q}}\hat{\mathbf{y}} + P_z{}^{\mathrm{NLoS}}\big|_{\mathrm{Q}}\hat{\mathbf{z}},
\end{aligned} \tag{18}$$

and from the Snell's law, we obtain:

$$P_y{}^{(r)}\Big|_{\mathrm{Q}} = \left(-P_y{}^{(i)}\Big|_{\mathrm{Q}}\cos(2\gamma) + P_z{}^{(i)}\Big|_{\mathrm{Q}}\sin(2\gamma)\right)c_{\parallel}(\gamma) = P_y{}^{\mathrm{NLoS}}\big|_{\mathrm{Q}}, \tag{19}$$

and

$$P_z{}^{(r)}\Big|_{\mathrm{Q}} = \left(-P_y{}^{(i)}\Big|_{\mathrm{Q}}\sin(2\gamma) + P_z{}^{(i)}\Big|_{\mathrm{Q}}\cos(2\gamma)\right)c_{\perp}(\gamma) = P_z{}^{\mathrm{NLoS}}\big|_{\mathrm{Q}}, \tag{20}$$

where $c_{\parallel}(\gamma)$ and $c_{\perp}(\gamma)$ are the reflection coefficients on the local plane reflecting surface centered on Q point for parallel and orthogonal incidence, respectively.

From (19) and (20), we observe that the components along $\hat{\mathbf{y}}$ and $\hat{\mathbf{z}}$ of the incident Poynting's vector contribute to the mirror reflection in point Q. The new reflection components *i.e.*, $P_{y,y}^{(r)}$, $P_{y,z}^{(r)}$, $P_{z,y}^{(r)}$, and $P_{z,z}^{(r)}$, propagate towards the receiver with the same propagation characteristics of the incident components, as the propagation medium is the same of the direct path (LoS path). Therefore, such components will arrive at the receiving end with an amplitude proportional to that of the incident waves, as influenced from the reflection in point Q, but with the same propagation characteristics.

To determine W^{NLoS} for the generic Q point, we observe that if the receiving surface is $(-\hat{\mathbf{y}})$-oriented, only $P_{y,y}^{(r)}$ and $P_{z,y}^{(r)}$ will contribute, while W^{LoS} is determined via P_y (see Figure 1). These two quantities can be written implicitly as functions of the electric field, but to give an explicit form of these, the partial differential equation in (9) satisfied by the electric field must be solved. This can be done by writing the electric component as a factorized expression that is

$$E_1 = e_1(x)\, e_2(y)\, e_3(z)\,. \tag{21}$$

Under this hypothesis, the expression of W^{LoS} in (16) becomes:

$$W^{\mathrm{LoS}} = j\frac{e_2(d)}{2\omega}\left(\frac{de_2^*(y)}{dy}\right)\Bigg|_{y=d} N_1 - \frac{|e_2(d)|^2}{2}N_2, \tag{22}$$

where N_1 and N_2 are two scalar quantities *i.e.*,

$$\begin{cases} N_1 = \int\limits_{x_1}^{x_2}\int\limits_{z_1}^{z_2} \rho_{33}^* |e_1(x)|^2 |e_3(z)|^2 dxdz \\ N_2 = \int\limits_{x_1}^{x_2}\int\limits_{z_1}^{z_2} \underline{\rho}_{R3}^* \bullet \underline{\xi}_{R1}^* |e_1(x)|^2 |e_3(z)|^2 dxdz \end{cases} \tag{23}$$

where x_1, x_2, z_1, and z_2 are the extension limits of S_R.

Finally, to determine W^{NLoS} at the receiving end, we observe that it can be written as the sum of infinite individual contributions of Q and R reflecting points $P_{y,k}^{\mathrm{NLoS}}$, but can be approximated to N_T element with $k = \{1, 2, \ldots, N_T\}$, over S_R:

$$W^{\mathrm{NLoS}} = \sum_{h=1}^{N_T} \int_{S_R} \hat{\mathbf{n}} \bullet \mathbf{P}_h{}^{(r)} dS = \sum_{h=1}^{N_T} \int_{S_R} \hat{\mathbf{n}} \bullet \left(P_{y,h}^{\mathrm{NLoS}} \hat{\mathbf{y}} + P_{z,h}^{\mathrm{NLoS}} \hat{\mathbf{z}} \right) dS. \quad (24)$$

To give a simplified example, we can consider the case of a single reflecting Q point (*i.e.*, $h = 1$), by assuming again that the $\hat{\mathbf{x}}$-polarized electric field is written in a factorized form. Following this hypothesis, we obtain:

$$W^{\mathrm{NLoS}}\big|_{h=1} = e_2(d) \int_{x_1}^{x_2} \int_{z_1}^{z_2} \left[\begin{array}{l} \frac{j}{\omega} \left(\rho_{33}^* \frac{de_2^*(y)}{dy}\Big|_{y=d} + \rho_{23}^* \frac{de_2^*(y)}{dz}\Big|_{y=d} \right) + \\ - \left(\underline{\rho}_{R3}^* + \underline{\rho}_{R2}^* \right) \bullet \underline{\xi}_{R1}^* e_2^*(d) \end{array} \right] |e_1(x)|^2 |e_3(z)|^2 dx dz. \quad (25)$$

Finally, from (16) and (25), the total power W, due to the contribution of a single generic reflection point, at the receiver is computed as $W|_{h=1} = W^{\mathrm{LoS}} + W^{\mathrm{NLoS}}\big|_{h=1}$.

We can conclude that all the remarks regarding the specific features of chiral metamaterials permit us to characterize them as perfect candidates for nanosystem applications realization, and more specifically, they represent the ideal candidates for operations in the THz and also higher frequencies. In fact, in comparison to natural materials, chiral metamaterials show strong response to the THz radiation that shows a very great technological potential in several sectors such as imaging, sensing and also communications. Also, materials exhibiting a giant tunable

optical activity show a very great potential in the achievement of active THz polarization components (such for example tunable polarizers, polarization filters, etc.). As outlined by Kenanakis *et al.* in [22], giant optical activity is a very important property particularly in the THz regime where there is a lack of optical components.

3. Equivalent Channel Model

In this section, we will present a channel model for THz band, based on ray tracing technique, and that considers the chirality effects of the EM field by taking advantage of the results in Section 2. Indeed, we firstly derived the received electric power in LoS and NLoS propagation in a chiral metamaterial from Maxwell's equations for the specific material. In this section we keep on exploiting Maxwell's equations to obtain the chirality dependence of the channel transfer functions in LoS and NLoS scenarios. More details on how the chirality affects the channel transfer functions are provided in the Appendix at the end of the paper.

The use of ray tracing techniques for channel modeling in THz band has been already adopted in [4], where the authors present a multi-ray propagation model consisting of LoS, reflected, scattered, and diffracted paths. Indeed, due to the very short wavelength in the THz band, the ray tracing approach allows accurate modeling. We refer to the work in [4], and consider the chirality effects on the channel impulse response, affecting both the LoS and NLoS ray propagation in the simplified case of spatial homogeneous chirality. The channel model will be the combination of many individual narrow sub-bands with a flat-band response. In the i-th frequency sub-band, the narrow-band channel impulse response

is expressed as a superposition of N_i rays, among which the n-th ray experiences frequency-dependent attenuation $\alpha_{i,n}$ that is also affected by chirality effects of the propagation medium.

In the case of stationary environment, with a fixed transmitter and receiver, the channel response of the multi-ray model is given as

$$h_i(\tau) = \sum_{n=1}^{N_i} \alpha_{i,n} \delta(\tau - \tau_n), \tag{26}$$

where τ and τ_n are the propagation delays for the direct ray, and the n-th NLoS ray, respectively.

Analogously in [4], by assuming a homogeneous chirality-affected LoS propagation, and $N_{\mathrm{Ref}}^{(i)}$ reflected rays, the multi-ray channel model in the i-th frequency sub-band can be described as:

$$h_i(\tau) = \alpha_{i,\mathrm{LoS}} \delta(\tau - \tau_{\mathrm{LoS}}) \mathbf{I}_{\mathrm{LoS}} + \sum_{l=1}^{N_{\mathrm{Ref}}^{(i)}} \alpha_{i,l}^{(\mathrm{Ref})} \delta\left(\tau - \tau_l^{(\mathrm{Ref})}\right), \tag{27}$$

where $\mathbf{I}_{LoS}$ is the indicator function that is equal to 1 or 0 for the presence of LoS path or not, respectively. For the LoS path, α_{LoS} and τ_{LoS} refer to the attenuation and the delay, respectively. For the l-th reflected path, $\alpha_{i,l}^{(\mathrm{Ref})}$, and $\tau_l^{(\mathrm{Ref})}$ correspond to the attenuation and the delay, respectively.

Through the use of Wiener-Khinchin theorem, the attenuations and delays in the i-th frequency sub-band can be expressed by the module of transfer functions H_{LoS}, and H_{NLoS}, respectively as LoS, and NLoS (*i.e.*, reflected) propagation paths.

The chirality-affected LoS channel transfer function can be expressed as:

$$H_{\mathrm{LoS}}(f) = H_{\mathrm{Abs}}(f)\, H_{\mathrm{Spr}}(f)\, e^{-j2\pi f \tau_{\mathrm{LoS}}}, \tag{28}$$

where H_{Abs} is the transfer function due to the molecular absorption loss that accounts for the attenuation that part of the wave energy is converted into internal kinetic energy to the molecules in the propagation medium [4], *i.e.*

$$H_{\mathrm{Abs}} = e^{-\frac{1}{2}k(f)d}, \tag{29}$$

while H_{Spr} is the transfer function due to the spreading loss, when the chirality is active *i.e.*,

$$H_{\mathrm{Spr}} = \frac{\nu_{\mathrm{Chir}}}{4\pi f d}, \tag{30}$$

by assuming d as the distance between the transmitter and the receiver. In (30), ν_{Chir} is the propagation velocity of the EM field in a chiral homogeneous isotropic medium *i.e.*,

$$\nu_{\mathrm{Chir}} = \frac{c}{n_{\mathrm{Chir}}}, \tag{31}$$

where n_{Chir} is the refractive index, and being $c = 1/\left(\sqrt{\varepsilon_0 \mu_0}\right)$, we can write

$$n_{\mathrm{Chir}} = \sqrt{\mu_r \varepsilon_r + \xi_{cr}^2}. \tag{32}$$

where ξ_{cr} is the relative chirality parameter, and ε_r (μ_r) is the relative electric (magnetic) permittivity (permeability), respectively. From (32), the expression in (31) becomes

$$\nu_{\mathrm{Chir}} = \frac{c}{\sqrt{\varepsilon_r \mu_r + \xi_{cr}^2}}. \tag{33}$$

Finally, it follows that $\tau_{\mathrm{LoS}} = d/\nu_{\mathrm{Chir}}$ is the time-of-arrival of the direct ray.

For the NLoS case, by considering d_1 as the distance between the transmitter and a generic reflecting point Q, and d_2 as the distance between Q and the receiver, the frequency-dependent transfer function of the NLoS ray propagation affected by the homogeneous chirality effect, *i.e.* H_{NLoS}, is given by [4]

$$H_{\mathrm{NLoS}}(f) = \left(\frac{\nu_{\mathrm{Chir}}}{4\pi f\,(d_1+d_2)}\right) e^{-j2\pi f\tau_{\mathrm{Ref}} - \frac{1}{2}k(f)(d_1+d_2)} \cdot R(f), \tag{34}$$

where $\tau_{\mathrm{NLoS}} = \tau_{\mathrm{LoS}} + (d_1+d_2-d)/\nu_{\mathrm{Chir}}$ is the time-of-arrival of the reflected ray, and $R(f)$ is the rough surface reflection loss of EM waves at THz band. It depends on the material, the shape and the roughness of the surface on which EM field has been reflected.

According to the Kirchhoff scattering theory, the reflection coefficient for a rough surface can be obtained by multiplying the smooth surface reflection coefficient derived from the Fresnel equations, $\Psi(f)$, with the Rayleigh roughness factor $\varsigma(f)$, as

$$R(f) = \Psi(f)\varsigma(f), \tag{35}$$

where Ψ is chosen according to the polarization of the incident Poynting's vector, and can be approximated as:

$$\Psi(f) \approx -\exp\left(\frac{-2\cos(\beta_i)}{\sqrt{n_{\mathrm{Chir}}^2 - 1}}\right). \tag{36}$$

and the Rayleigh roughness factor is defined as:

$$\varsigma(f) = \exp\left(-\frac{8\pi^2 f^2 \sigma^2 \cos^2(\beta_i)}{\nu_{\mathrm{Chir}}^2}\right), \tag{37}$$

with σ as the rough surface height standard deviation, commonly assumed as Gaussian-distributed.

By combining the aforementioned models in (28) and (34), the channel model in the i-th frequency sub-band in (27) becomes as:

$$\begin{aligned} h_i(\tau) = & \left| \frac{\nu_{\text{Chir}}}{4\pi f_i d} e^{-\frac{1}{2}k(f_i)d} \right| \delta(\tau - \tau_{\text{LoS}}) \mathbf{I}_{\text{LoS}} + \\ & + \sum_{l=1}^{N_{\text{Ref}}^{(i)}} \left| \frac{\nu_{\text{Chir}}}{4\pi f_i (d_1+d_2)} e^{-\frac{1}{2}k(f_i)(d_1+d_2)} e^{-\frac{2\cos(\beta_i)}{\sqrt{n_{t,\text{Chir}}^2 - 1}}} e^{-\frac{8\pi^2 f_i^2 \sigma^2 \cos^2(\beta_i)}{\nu_{\text{Chir}}^2}} \right| \\ & \cdot \delta\left(\tau - \tau_l^{(\text{Ref})}\right). \end{aligned} \tag{38}$$

Now, we are able to compute the total path loss, *i.e.* A [dB], both in the case of LoS and NLoS propagation. In the first case, it is contributed by the spreading path loss (*i.e.*, A_s), and the absorption path loss (*i.e.*, A_a), and it can be expressed as:

$$A_{\text{LoS}} = A_s + A_a = 20\log_{10}\left(\frac{4\pi d}{\lambda_{\text{Chir}}}\right) + 10\gamma d \log_{10} e, \tag{39}$$

where $\lambda_{\text{Chir}} = \nu_{\text{Chir}}/f$ is the wavelength in the considered medium affected by the homogeneous chirality, and γ is the absorption coefficient measuring the amount of absorption loss of the EM field in the medium.

On the other hand, from (34) we can derive the total path loss for NLoS propagation *i.e.*, A_{NLoS}, as follows:

$$\begin{aligned} A_{\text{NLoS}} = & 20\log_{10}\left(\frac{\nu_{\text{Chir}}}{4\pi f(d_1+d_2)}\right) + \\ & + 20\log_{10}\left(e^{-\frac{1}{2}\alpha(d_1+d_2)} e^{-\frac{2\cos(\beta_i)}{\sqrt{n_{\text{Chir}}^2 - 1}}} e^{-\frac{8\pi^2 f^2 \sigma^2 \cos^2(\beta_i)}{\nu_{\text{Chir}}^2}} \right). \end{aligned} \tag{40}$$

4. Simulation Results

In this section, we distinguish simulation results for LoS and NLoS propagation models, in the case of (*i*) biological (for very small distances, in the order of millimeters), and (*ii*) indoor (for small distances, in the order of meters) wireless communications, and w.r.t. the chirality effects on these two types of propagation models. Since in this paper our aim is basically addressed to the path loss behavior in LoS and NLoS propagation (assuming reflected paths only) in a chiral affected medium, in the simulation results, we focus only on LoS and NLoS transfer functions with chirality effects, assuming a flat behavior for the molecular absorption loss (*i.e.*, frequency independent behavior). Thus, the following results represent the behavior of transmitted signals propagating along LoS and NLoS directions in a chirality-affected channel, by omitting the frequency-dependent molecular absorption effect.

In this framework, we discuss the influence of low values of chirality parameter *i.e.*, $\xi_{\text{Chir}} = 1$, separately from the higher values occurring in the GOA medium *i.e.*, $\xi_{\text{Chir}} = 10$.

Simulation results have been obtained under the assumption of homogeneous chirality and with a linear electric polarization. Standard values of the chiral parameter ξ_{Chir} have been chosen varying in the range $0 \leq |\xi_{\text{Chir}}| \leq 1$. However higher values for ξ_{Chir} have been considered [19, 20, 23, 24] to evaluate the effects of this parameter in the particular media such as the chiral complex materials where a giant optical activity with strong circular dichroism takes place. In this special media, $|\xi_{\text{Chir}}|$ can be extended up to $|\xi_{\text{Chir}}| \approx 5 \div 10$.

Table 1 collects the parameters used in the simulation results in the cases of LoS, NLoS, and GOA scenarios. Distance values are (*i*) $d = [1, 10]$ mm (m), and

Table 1: Parameters used in the simulations for LoS, NLoS, and GOA cases. Common parameters are $f = [0.06, 60]$ THz, $\varepsilon_0 = 8.85 \times 10^{-12}$, $\mu_0 = 4\pi 10^{-7}$.

Scenario	**Parameters**
LoS	$\varepsilon_r = [1, 3, 12]$ $\mu_r = 1$ $\xi_{\text{Chir}} = 1$ $\gamma = 0.6$
NLoS	$\varepsilon_r = [1, 3, 12]$ $\mu_r = 1$ $\xi_{\text{Chir}} = 1$ $\beta_1 = \pi/6$, $\sigma = 10^{-6}$
GOA	$\varepsilon_r = [40, 60, 80]$ $\mu_r = 40$ $\xi_{\text{Chir}} = 10$

(*ii*) $d_1 = d_2 = [1, 10]$ mm (m), for biological (indoor) LoS and NLoS scenarios, respectively. In GOA scenario, the values of ε_r have been chosen in accordance with [19]–[24]. In the following, we describe the simulation results for LoS, NLoS and GOA scenarios.

Figure 3 depicts the total path loss for LoS propagation in a biological environment in the frequency range $[0.06, 60]$ THz, and for different values of electrical permittivity ε_r corresponding to the case of (*i*) vacuum ($\varepsilon_r = 1$), (*ii*) calcium ($\varepsilon_r = 3$), and (*iii*) silicon ($\varepsilon_r = 12$). We observe that low values in ξ_{Chir}, *i.e.* $\xi_{\text{Chir}} = 1$, contribute to a lower rate of attenuation (*i.e.*, $< 60 - 80$ dB) in the lower THz band $[0.06, 10]$ THz, for observation points laying in the range of millimeters (see Figure 3 (*a*) and (*b*)). Graphs are plotted for same different values in the relative electric permittivity ε_r, and can be of some interest for a biological propagation medium. We also observe that path loss increases for higher values

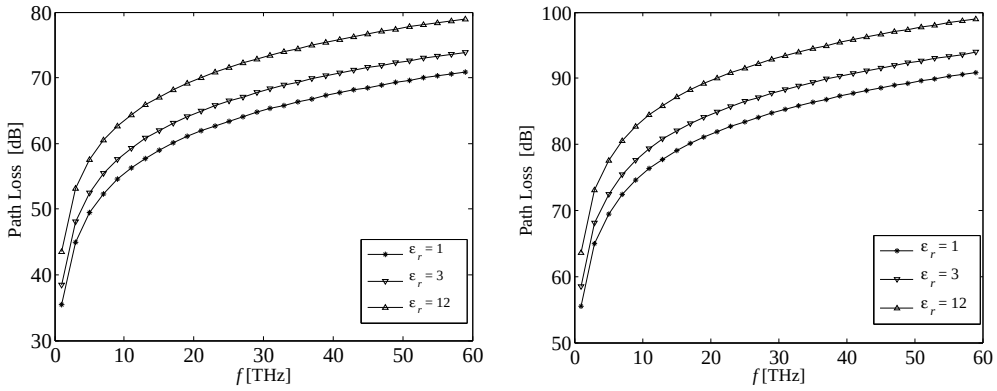

Figure 3: Total path loss for LoS propagation in a biological environment with a chirality-affected channel ($\xi_{\text{Chir}} = 1$), for (*a*) $d = 1$ mm, and (*b*) $d = 10$ mm.

of ε_r.

For LoS propagation effects in an indoor environment, Figure 4 (*a*) and (*b*) referred to $\xi_{\text{Chir}} = 1$ and $d = 1$, and $d = 10$ m, respectively, show similar behaviors but with different dynamicity in the lower THz band. Specifically, in the range $[0.06, 10]$ THz, the attenuation values span from $[100, 125]$ dB to $[140, 170]$ dB, respectively in Figure 4 (*a*), and (*b*).

In NLoS propagation case, we have a similar behavior as those observed in LoS propagation. Figure 5 regarding the propagation in bio-media shows small variations for different values of ε_r, with levels of attenuation higher than those exhibited in the LoS propagation scenario. In fact, in Figure 5 (*a*) we observe a path loss ranging around $[30, 90]$ dB, while values increase for higher distances as depicted in Figure 5 (*b*) for indoor environment. A similar behavior is observed in Figure 6 related to indoor NLoS propagation, where the path loss graphs are higher w.r.t. the values in the biological scenario, *i.e.*, they lay in the ranges $\approx$

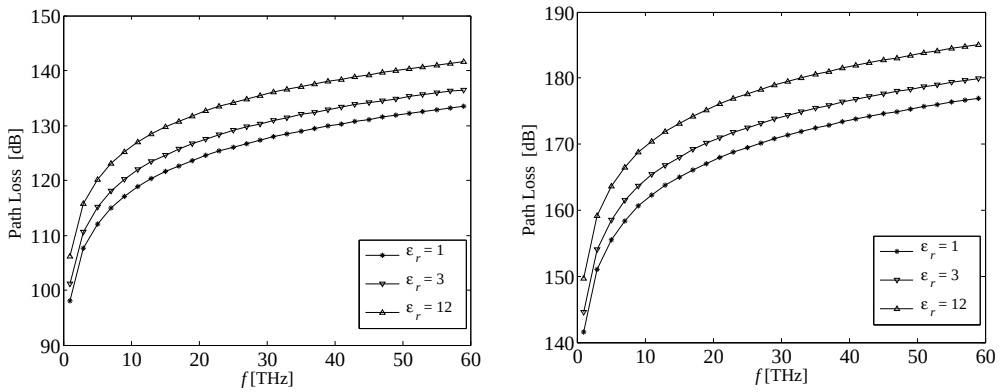

Figure 4: Total path loss for LoS propagation in an indoor environment with a chirality-affected channel ($\xi_{\text{Chir}} = 1$), for (*a*) $d = 1$ m, and (*b*) $d = 10$ m.

$[95, 155]$ dB and $\approx [160, 225]$ dB for $d_1 = d_2 = 1$ m, and $d_1 = d_2 = 10$ m, respectively.

Finally, we investigate the path loss for LoS and NLoS scenarios in media that exhibit high values of ξ_{Chir}, that is when the environment where the electromagnetic field is propagating is a chiral unconventional material (Chiral Meta-Material). In Figure 7 we observe a reduction of the attenuation in the band $[0.06, 10]$ THz w.r.t the remaining (higher) THz band, but with higher levels of path loss. Furthermore, it is observed [19, 20, 23, 24] that the GOA produces also a growth in the effective values of ε_r and μ_r. This difference in the values of ξ_{Chir} is due to the higher electromagnetic interactions that arise when the doping impurities (cross-wire structures) are used in GOA materials.

In the case of GOA scenario and indoor LoS propagation (Figure 8), we observe again low attenuation levels in $[0.06, 10]$ THz but with a fast dynamicity $\approx [130, 150]$ dB for $d = 1$ m, and $[170, 190]$ dB for $d = 10$ m. Finally, for NLoS

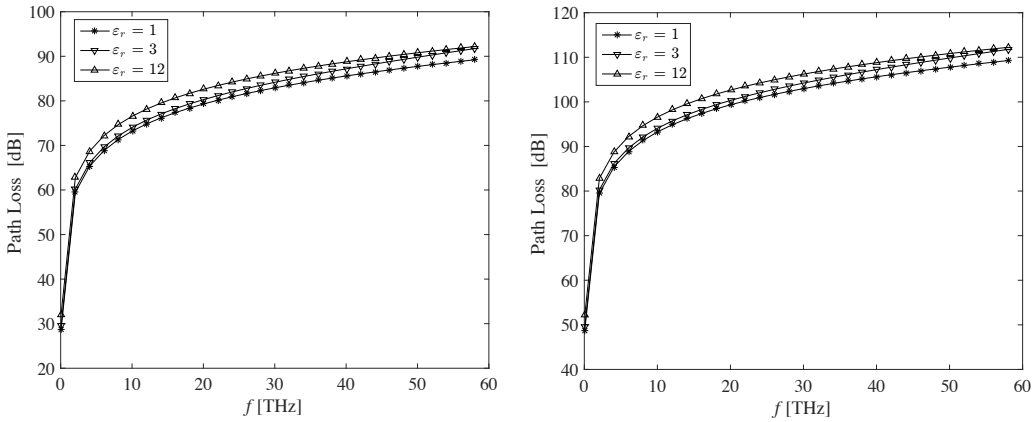

Figure 5: Total path loss for NLoS propagation in a biological environment with a chirality-affected channel ($\xi_{\text{Chir}} = 1$), for (*a*) $d_1 = d_2 = 1$ mm, and (*b*) $d_1 = d_2 = 10$ mm distance.

scenario with GOA effect, we notice low values of path loss for lower frequencies, while increasing trends are observed with higher frequency range, both for the biological and indoor cases (see Figure 9 and Figure 10, respectively). In the typical range of Terahertz nanocommunications *i.e.*, $[0.06, 10]$ THz, NLoS path loss with GOA has low and almost flat values, thus representing an efficient transmission scenario. For higher frequencies, the behavior is strongly dependent on the relative electrical permittivity, and then on the specific features of the transmission material.

To summarize, we can conclude that chirality effects act differently on the LoS path and on the NLoS path. Specifically, low values affect the LoS attenuation with a progressive increase for higher frequency range up to 60 THz, and this effect is more consistent with the growth in the values of ε_r. Higher values are also experienced for higher distances (indoor scenario). For a better understanding

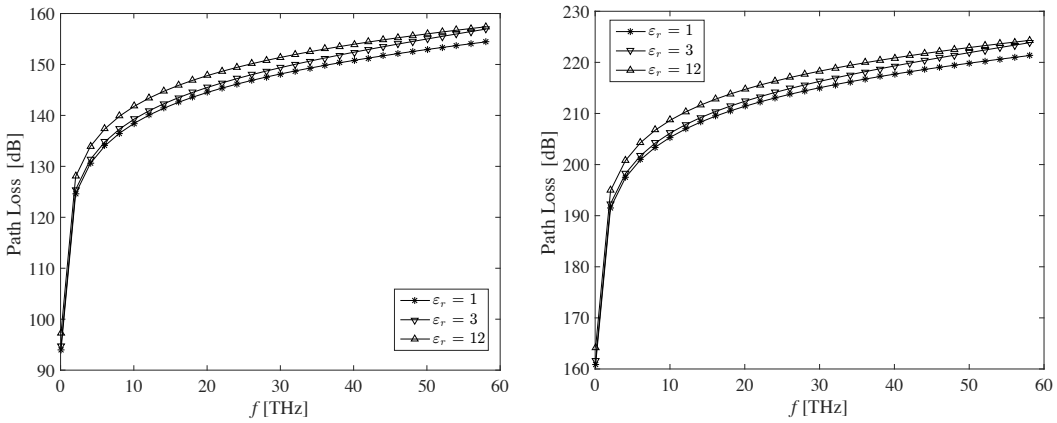

Figure 6: Total path loss for NLoS propagation in an indoor environment with a chirality-affected channel ($\xi_{\text{Chir}} = 1$), for (*a*) $d_1 = d_2 = 1$ m, and (*b*) $d_1 = d_2 = 10$ m distance.

of the obtained results, Table 2 collects the path loss values for different scenarios in the lower frequency range *i.e.*, $[0.06, 10]$ THz. Different is the situation in NLoS scenario. In fact the impact of the chirality factor is well hidden by the presence of the scattered rays through the high values associated to the Rayleigh roughness factor. This means that a chiral medium is more sensible to an incident reflected electromagnetic field than to a scattered one. Finally, in all the scenarios with GOA the path loss shows on average higher values w.r.t. the cases without GOA. However, small variations occur in NLoS at lower THz frequencies *i.e.*, $[0.06, 10]$ THz, while very high values are for increasing frequencies. This highlights the possibility to use chiral metamaterials with GOA as transmission channels in the low THz frequency range.

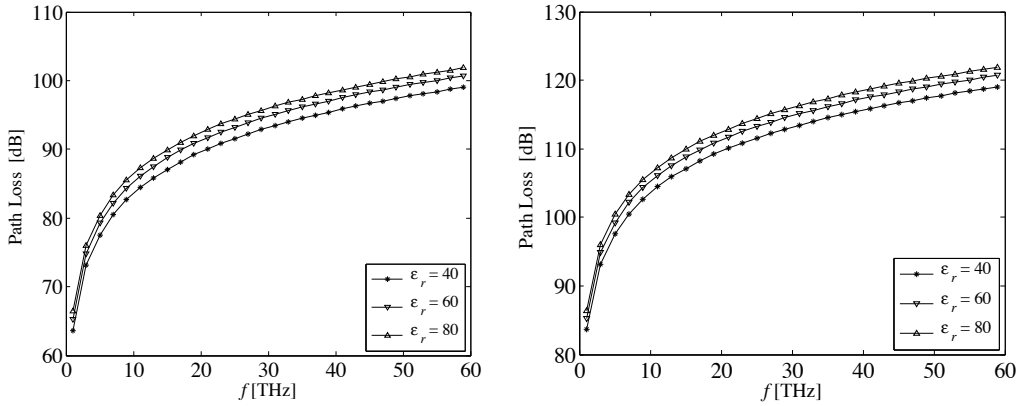

Figure 7: Total path loss for LoS propagation in a biological environment with GOA effect ($\xi_{\rm Chir} = 10$), for (*a*) $d = 1$ mm, and (*b*) $d = 10$ mm. ε_r and μ_r effective values have been chosen in accordance with [19]- [24].

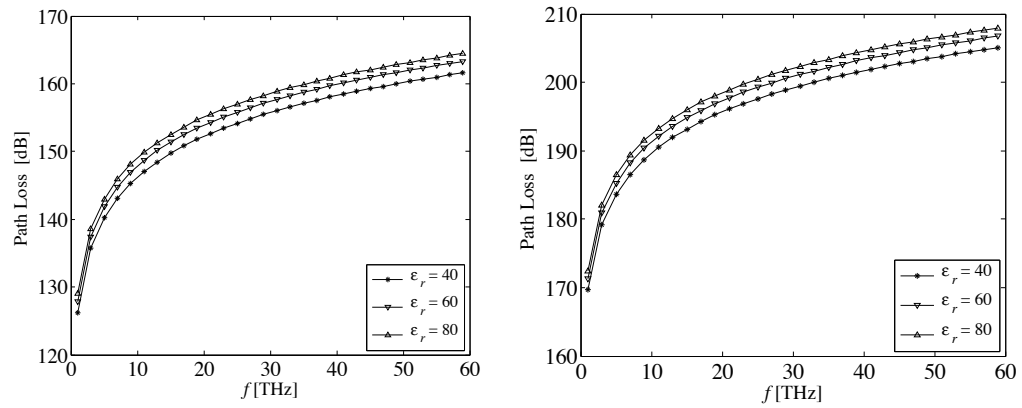

Figure 8: Total path loss for LoS propagation in an indoor environment with GOA effect ($\xi_{\rm Chir} = 10$), for (*a*) $d = 1$ m, and (*b*) $d = 10$ m. ε_r and μ_r effective values have been chosen in accordance with [19]– [24].

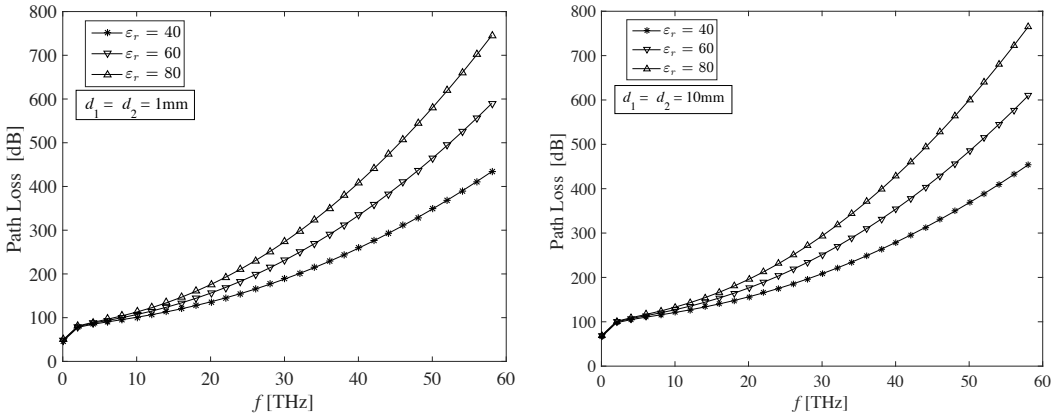

Figure 9: Total path loss for NLoS propagation in a biologic environment with GOA effect ($\xi_{\text{Chir}} = 10$), for (*a*) $d_1 = d_2 = 1$ mm, and (*b*) $d_1 = d_2 = 10$ mm. ε_r and μ_r effective values have been chosen in accordance with [19]- [24].

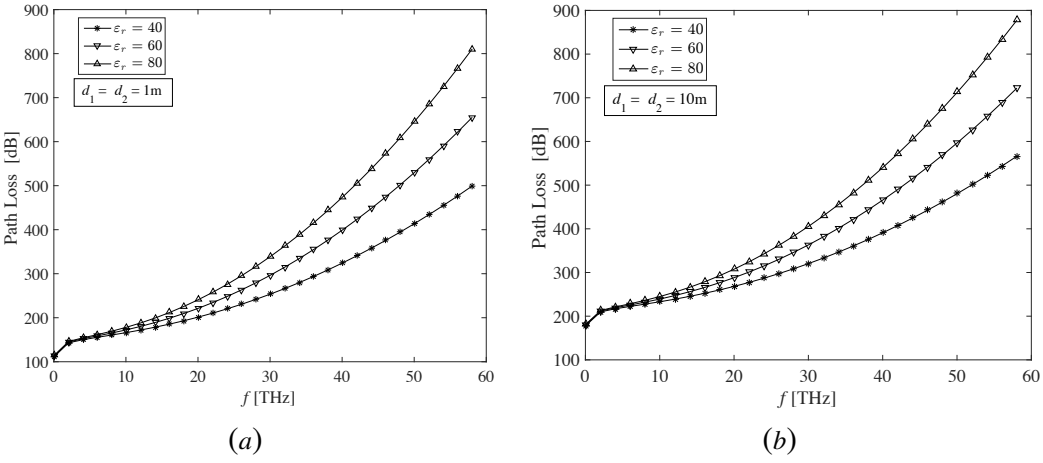

Figure 10: Total path loss for NLoS propagation in an indoor environment with GOA effect ($\xi_{\text{Chir}} = 10$), for (*a*) $d_1 = d_2 = 1$ m, and (*b*) $d_1 = d_2 = 10$ m. ε_r and μ_r effective values have been chosen in accordance with [19]- [24].

Table 2: Approximated path loss results obtained for LoS, NLoS, and GOA cases in the frequency range $[0.06, 10]$ THz and for different distances.

Scenario	**Biological**	**Indoor**
LoS	$[35, 60]$ dB, for $d = 1$ mm $[55, 85]$ dB, for $d = 10$ mm	$[100, 125]$ dB, for $d = 1$ m $[140, 170]$ dB, for $d = 10$ m
NLoS	$[30, 75]$ dB, for $d_1 = d_2 = 1$ mm $[50, 95]$ dB, for $d_1 = d_2 = 10$ mm	$[95, 140]$ dB, for $d_1 = d_2 = 1$ m $[160, 210]$ dB, for $d_1 = d_2 = 10$ m
GOA, LoS	$[65, 85]$ dB, for $d = 1$ mm $[85, 105]$ dB, for $d = 10$ mm	$[130, 150]$ dB, for $d = 1$ m $[170, 190]$ dB, for $d = 10$ m
GOA, NLoS	$[50, 102]$ dB, for $d_1 = d_2 = 1$ mm $[80, 105]$ dB, for $d_1 = d_2 = 10$ mm	$[100, 190]$ dB, for $d_1 = d_2 = 1$ m $[198, 230]$ dB, for $d_1 = d_2 = 10$ m

5. Conclusions

In this paper, we have presented a theoretical approach to evaluate the chirality effects on the electromagnetic propagation in a real complex medium. A full-wave model has been considered and the electromagnetic field has been studied in the THz frequency band with particular emphasis on the determination of the W^{LoS} and W^{NLoS} power terms.

Chirality has been shown to be responsible of low attenuation in LoS propagation, while it increases for NLoS scenario due to the the presence of the reflected rays in two types of environment considered (*i.e.*, biological and indoor applications). Finally, in the case of GOA both in LoS and NLoS, the path loss has a flat behavior for lower frequencies (*i.e.*, < 10 THz).

Appendix

The Maxwell's equations for the harmonic non-conventional medium defined under the hypothesis of plane wave become:

$$\begin{cases} \mathbf{k} \times \mathbf{E_0} = \omega\xi\mathbf{E_0} + \omega\mu\mathbf{H_0} \\ \mathbf{k} \times \mathbf{H_0} = -\omega\varepsilon\mathbf{E_0} - \omega\zeta\mathbf{H_0} \end{cases} \tag{41}$$

By posing the magnetic field as

$$\mathbf{H_0} = \frac{1}{\omega\mu}\mathbf{k} \times \mathbf{E_0} - \frac{\xi}{\mu}\mathbf{E_0}, \tag{42}$$

we obtain

$$\mathbf{k}\mathbf{k}\cdot\mathbf{E_0}-\omega\left(\xi-\zeta\right)\mathbf{k}\times\mathbf{E_0}+\omega^2\left(\mu\varepsilon-\xi\zeta-\mathbf{k}\cdot\mathbf{k}\right)\mathbf{E_0}=0, \tag{43}$$

with $\mathbf{k}\cdot\mathbf{k}=k^2$, where k is the complex amplitude of the propagation vector $\mathbf{k}$.

In order to find the dispersion relation, we need to compute $\mathbf{k}\cdot\mathbf{E_0}$, and then we have to consider the divergence equations for both the electrical and magnetic displacement $\mathbf{D_0}$ and $\mathbf{B_0}$, respectively. Those equations arise to the following linear homogeneous system of two equations for the unknown quantities $\mathbf{k}\cdot\mathbf{E_0}$, and $\mathbf{k}\cdot\mathbf{H_0}$:

$$\begin{cases}\mathbf{k}\cdot\mathbf{B_0}=\xi\mathbf{k}\cdot\mathbf{E_0}+\mu\mathbf{k}\cdot\mathbf{H_0}=0\\ \mathbf{k}\cdot\mathbf{D_0}=\varepsilon\mathbf{k}\cdot\mathbf{E_0}+\zeta\mathbf{k}\cdot\mathbf{H_0}=0\end{cases} \tag{44}$$

We notice that the system in (44) provides (*i*) ∞^1 autosolutions for $\mathbf{k}\cdot\mathbf{E_0}\neq 0$, $\mathbf{k}\cdot\mathbf{H_0}\neq 0$, if and only if

$$\mu\varepsilon-\xi\zeta=0, \tag{45}$$

and (*ii*) trivial solutions $\mathbf{k}\cdot\mathbf{E_0}=0$, $\mathbf{k}\cdot\mathbf{H_0}=0$, if and only if

$$\mu\varepsilon-\xi\zeta\neq 0. \tag{46}$$

It is evident that only trivial solutions are acceptable. Indeed, Eq. (46) is never

verified since

$$\begin{cases} \xi = \xi_0 \xi_r \\ \mu = \mu_0 \mu_r \\ \varepsilon = \varepsilon_0 \varepsilon_r \\ \zeta = \zeta_0 \zeta_r \end{cases} \tag{47}$$

and by assuming a reciprocal material *i.e.*,

$$\xi = \zeta \Rightarrow j\xi_0\xi_r = j\zeta_0\zeta_r, \tag{48}$$

we get $\xi_r > 0$, and $\zeta_r > 0$. So, we can deduce that (46) becomes

$$\mu\varepsilon - \xi\zeta = 0 \Rightarrow \mu_0\mu_r\varepsilon_0\varepsilon_r - j\xi_0\xi_r j\zeta_0\zeta_r = 0 \Rightarrow \mu_0\mu_r\varepsilon_0\varepsilon_r + \xi_0^2\xi_r^2, \tag{49}$$

and this is never null except for Single NeGative (SNG) materials, which are not considered in this paper.

By assuming a reciprocal material, (46) is not verified, and only the trivial solutions are acceptable. It follows that $\mathbf{k} \cdot \mathbf{E_0} = 0$, $\mathbf{k} \cdot \mathbf{H_0} = 0$ and then, based on previous hypothesis, the dispersion relation becomes:

$$\mathbf{kk}\cdot\mathbf{E_0} - \omega\left(\xi - \zeta\right)\mathbf{k}\times\mathbf{E_0} + \omega^2\left(\mu\varepsilon - \xi\zeta - k^2\right)\mathbf{E_0} = 0 \Rightarrow \omega^2\left(\mu\varepsilon - \xi\zeta - k^2\right) = 0, \tag{50}$$

The values of k derive from (50) as:

$$\mu\varepsilon - \xi\zeta - k^2 = 0, \tag{51}$$

1 that is

$$k = \pm\sqrt{\mu_0\mu_r\varepsilon_0\varepsilon_r + \xi_0^2\xi_r^2} = \pm\sqrt{\mu_0\varepsilon_0\left(\varepsilon_r\mu_r + \xi_r^2\right)} = \pm\sqrt{\mu_0\varepsilon_0}\sqrt{\varepsilon_r\mu_r + \xi_r^2},$$

2 (52)

3 being $\xi_0 = \sqrt{\mu_0\varepsilon_0}$. It follows that the propagation vector will be:

4 $$\mathbf{k} = \pm\sqrt{\mu_0\varepsilon_0}\sqrt{\varepsilon_r\mu_r + \xi_r^2}\hat{\mathbf{k}}. \tag{53}$$

5 Finally, the amount ν_{Chir} is the relative refractive index for a reciprocal material
6 (except SNG), whose expression is:

7 $$\nu_{\text{Chir}} = \sqrt{\varepsilon_r\mu_r + \xi_r^2}. \tag{54}$$

8

References

[1] R. Piesiewicz, T. Kleine-Ostmann, N. Krumbholz, D. Mittleman, M. Koch, J. Schoebel, T. Kurner, Short-Range Ultra-Broadband Terahertz Communications: Concepts and Perspectives, Antennas and Propagation Magazine, IEEE 49 (6) (2007) 24–39. doi:10.1109/MAP.2007.4455844.

[2] T. Kurner, S. Priebe, Towards THz Communications - Status in Research, Standardization and Regulation, Journal of Infrared, Millimeter, and Terahertz Waves 35 (1) (2014) 53–62. doi:10.1007/s10762-013-0014-3.
URL `http://dx.doi.org/10.1007/s10762-013-0014-3`

[3] A. Moldovan, M. Ruder, I. Akyildiz, W. Gerstacker, LOS and NLOS

channel modeling for terahertz wireless communication with scattered rays, in: Globecom Workshops (GC Wkshps), 2014, 2014, pp. 388–392. doi:10.1109/GLOCOMW.2014.7063462.

[4] C. Han, A. Bicen, I. Akyildiz, Multi-Ray Channel Modeling and Wideband Characterization for Wireless Communications in the Terahertz Band, Wireless Communications, IEEE Transactions on 14 (5) (2015) 2402–2412. doi:10.1109/TWC.2014.2386335.

[5] J. Jornet, I. Akyildiz, Channel Modeling and Capacity Analysis for Electromagnetic Wireless Nanonetworks in the Terahertz Band, Wireless Communications, IEEE Transactions on 10 (10) (2011) 3211–3221. doi:10.1109/TWC.2011.081011.100545.

[6] I. Llatser, A. Mestres, S. Abadal, E. Alarcon, H. Lee, A. Cabellos-Aparicio, Time- and Frequency-Domain Analysis of Molecular Absorption in Short-Range Terahertz Communications, Antennas and Wireless Propagation Letters, IEEE 14 (2015) 350–353. doi:10.1109/LAWP.2014.2362194.

[7] G. Piro, K. Yang, G. Boggia, N. Chopra, L. Grieco, A. Alomainy, Terahertz Communications in Human Tissues at the Nanoscale for Healthcare Applications, Nanotechnology, IEEE Transactions on 14 (3) (2015) 404–406. doi:10.1109/TNANO.2015.2415557.

[8] P. Boronin, D. Moltchanov, Y. Koucheryavy, A molecular noise model for THz channels, in: Communications (ICC), 2015 IEEE International Conference on, 2015, pp. 1286–1291. doi:10.1109/ICC.2015.7248500.

[9] J. Kokkoniemi, J. Lehtomki, M. Juntti, A discussion on molecular absorption noise in the terahertz band, Nano Communication Networks (2015) –doi:http://dx.doi.org/10.1016/j.nancom.2015.11.001.
URL http://www.sciencedirect.com/science/article/pii/S1878778915000472

[10] F. Sheikh, M. El-Hadidy, T. Kaiser, Terahertz band: Indoor ray-tracing channel model considering atmospheric attenuation, in: Antennas and Propagation USNC/URSI National Radio Science Meeting, 2015 IEEE International Symposium on, 2015, pp. 1782–1783. doi:10.1109/APS.2015.7305280.

[11] R. Piesiewicz, C. Jansen, D. Mittleman, T. Kleine-Ostmann, M. Koch, T. Kurner, Scattering Analysis for the Modeling of THz Communication Systems, Antennas and Propagation, IEEE Transactions on 55 (11) (2007) 3002–3009. doi:10.1109/TAP.2007.908559.

[12] J. Kokkoniemi, J. Lehtomaki, K. Umebayashi, M. Juntti, Frequency and Time Domain Channel Models for Nanonetworks in Terahertz Band, Antennas and Propagation, IEEE Transactions on 63 (2) (2015) 678–691. doi:10.1109/TAP.2014.2373371.

[13] A. Sihvola, Metamaterials in electromagnetics, Metamaterials 1 (1) (2007) 2–11.

[14] G. Kenanakis, E. N. Economou, C. M. Soukoulis, M. Kafesaki, Controlling THz and far-IR waves with chiral and bianisotropic metamaterials, EPJ Applied Metamaterials 2 (2015) 15. doi:10.1051/epjam/2015019.
URL http://dx.doi.org/10.1051/epjam/2015019

[15] K. Lindman, Om en genom ett isotropt system av spiralformiga resonatorer alstrad rotationspolarisation av elektromagnetiska vagorna, Ofversigt af Finska Vetenskaps-Societetens forhandlingar, A. Matematik och naturvetenskaper LVII (3) (1914-1915) 1–32.

[16] N. Engheta, Chiral Materials and Chiral Electrodynamics: Background & Basic Physical Principles, in: Special Workshop on Chiral and Complex Materials Progress in Electromagnetics Research Symposium (PIERS'91), Cambridge, Massachusetts, 1991.

[17] A. Lakhtakia, Recent contributions to classical electromagnetic theory of chiral media: what next?, Speculations in Science and Technology 14 (1) (1991) 2–17.

[18] I. Lindell, A. Sihvola, S. Tretyakov, A. Viitanen, Electromagnetic waves in chiral and bi-isotropic media, Artech House, 1994.

[19] F. Fang, Y. Cheng, Dual-band Terahertz Chiral Metamaterial with Giant Optical Activity and Negative Refractive Index based on Cross-wire Structure, Progress In Electromagnetics Research M 31 (2013) 59–69.

[20] J. Zhou, D. R. Chowdhury, R. Zhao, A. K. Azad, H.-T. Chen, C. M. Soukoulis, A. J. Taylor, J. F. O'Hara, Terahertz chiral metamaterials with giant and dynamically tunable optical activity, Phys. Rev. B 86 (2012) 035448. doi:10.1103/PhysRevB.86.035448.
URL http://link.aps.org/doi/10.1103/PhysRevB.86.035448

[21] J. Kong, Electromagnetic Wave Theory, A Wiley-Interscience publication, Wiley, 1986.
URL https://books.google.it/books?id=OposAAAAYAAJ

[22] G. Kenanakis, R. Zhao, N. Katsarakis, M. Kafesaki, C. M. Soukoulis, E. N. Economou, Optically controllable THz chiral metamaterials, Opt. Express 22 (10) (2014) 12149–12159. doi:10.1364/OE.22.012149.
URL http://www.opticsexpress.org/abstract.cfm?URI=oe-22-10-12149

[23] R. Zhao, T. Koschny, C. M. Soukoulis, Chiral Metamaterials: retrieval of the effective parameters with and without substrate, Optics express 18 (4).

[24] G. Kenanakis, R. Zhao, A. Stavrinidis, G. Konstantinidis, N. Katsarakis, M. Kafesaki, C. M. Soukoulis, E. N. Economou, Flexible Chiral Metamaterials in the Terahertz Regime: a Comparative Study of Various Designs, Opt. Mater. Express 2 (12) (2012) 1702–1712. doi:10.1364/OME.2.001702.
URL http://www.osapublishing.org/ome/abstract.cfm?URI=ome-2-12-1702